**FULL PAPER**

# Metal Nanoparticles Acting as Light-Activated Heating Elements within Composite Materials

*Somsubhra Maity, Jason R. Bochinski, and Laura I. Clarke\**

The photothermal effect of metal nanoparticles embedded in polymeric materials can be used to efficiently generate local heat for in situ thermally processing within an existing material. Fluorescent probes are employed as thermal sensors to allow dynamical measurement of the amplitude and rate of temperature change within the polymer matrix. The efficacy of this technique is demonstrated in polymer nanocomposite samples with different morphological characteristics, namely nanofibrous mats and thin film samples. For similarly thick materials and both types of sample morphology, average temperature increases on the order of ≈100s °C are readily obtained with dilute nanoparticle concentrations under relatively low irradiation intensity. Thus, the in situ photothermal heating approach has great potential for controllably driving a multitude of thermal processes, such as triggering phase transitions, generating site-specific cross-linking, or initiating chemical reactions from within a material.

## 1. Introduction

Metal nanoparticles are ubiquitous in chemistry, biology, physics, and nanoscale science research[1] studies due to their facile fabrication[2,3] and powerful electronic[4] and optical properties.[5] These useful capabilities are consequences of the particle's material composition coupled with its small size.[6] Myriad technological applications have been proposed or developed for nanoparticles: a short list of diverse examples includes nanophotonic devices,[7] enhancers for biological spectroscopy[8] and imaging,[9] biochemical sensors,[10] or acting as nanoscale electronic components in fundamental charge transfer[11] and transport studies.[12–16] Interestingly, one property of metal nanoparticles previously considered detrimental but now recognized as potentially very useful[17,18] is the photothermal effect, that is, the ability to efficiently convert optical energy into local heat.

Much work involving such light-driven heating has occurred in aqueous environments, where the photothermal effect has been utilized for biomedical applications[19–22] such as targeted substance release[23–26] or cancer therapy.[27–32] In these biological settings, experiments commonly utilize high intensity excitation light from short pulsed lasers spectrally tuned to the near infrared region; such application of intense excitation can locally heat nanoparticles to extreme temperatures, generating bubbles from vaporizing fluid[33,34] or even reshaping the metal objects themselves.[35]

In general, beyond the aforementioned specific applications, the capability to controllably apply heat at multiple nanoscale locations in the interior of an object has obvious potential utility for a multitude of additional uses such as triggering phase transitions,[36] generating site-specific cross-linking, or initiating chemical reactions from within a material. With this photothermal effect, the application of light resonant with the surface plasmon of a metal nanoparticle creates heating of the immediate surrounding region through a sequence of cascading events: the light excites the plasmon and rapid electron-phonon scattering dissipates this energy within the nanoparticle, raising its temperature and providing a point-like source of heat. This energy is subsequently released from the particle surface into the surrounding medium, and the entire process repeated. Moreover, when embedded in a matrix (e.g., a polymeric material), the specificity of the interaction between the metal nanoparticle and the light field allows for this heat generation to be initiated only at the nanoparticle locations with minimal coupling between the light and the remainder of the solid. This condition is readily achieved with appropriate tuning of the nanoparticle surface plasmon resonance (SPR) frequency (by altering nanoparticle composition, size, or shape) to lie within spectral transmission bands of the material matrix, enabling the nanoparticle thermal energy sources placed within samples to generate heating of the interior without first needing to warm the surface. Thus, this plasmon-mediated generation of heat without direct physical contact is internal, spatially selective, and (initially) highly localized.

In contrast to the aforementioned reported progress in biomedical research, much less work has appeared using the photothermal effect of metal nanoparticles within solid phase materials.[36–40] Earlier our group reported experimental observations of photothermal heating by means of a dilute concentration of gold nanoparticles homogeneously embedded within nanofibrous polymeric structures[41] which exhibited gradual global temperature increases of ≥50 °C when the sample was irradiated with weak green light (532 nm at 0.10 W/cm², which, for scale, we note is approximately the intensity of a common laser pointer). This remotely actuated heating ultimately resulted in

S. Maity, Prof. J. R. Bochinski, Prof. L. I. Clarke
Department of Physics
NC State University
2401 Stinson Drive, Box 8202
Raleigh, NC 27695-8202, USA
E-mail: laura_clarke@ncsu.edu

destructive melting of the nanofibrous material. In the current report, we describe achieving a more extensive temperature increase in polymeric samples with different morphologies (thin films as well as nanofibrous mats), measured utilizing a non-invasive optical thermometer. Based on the relative emission change of a fluorescent molecule, the average temperature of the sample's interior can be determined rapidly, remotely, and without necessitating sample damage. We discuss changes in the heating rate and attained steady-state temperature as a function of material type, sample morphology, and laser intensity, correlating the internal temperature measurements with previous observations of melting in nanofibrous systems. These results demonstrate that significant heating is readily achieved in thin solid (fibrous or non-fibrous) polymeric systems, even when utilizing a relatively weak intensity of irradiation; controlling the balance between heating rate and thermal loss mechanisms can maximize the attained average internal sample temperature (for a fixed nanoparticle concentration and laser intensity).

## 2. Results and Discussion

### 2.1. Measurement of Average Sample Temperature via Fluorescence

Fluorescent molecules (perylene) were utilized as nanoscale thermometers to measure the temperature increase due to nanoparticle plasmon-mediated heating within thin films and nanofibrous mats. The fluorophores are randomly distributed within the sample and not tethered to a particular site along the polymer chain. When acting as such a dilute sensor, perylene exhibits multiple vibrational absorption peaks within the electronic $S_0$–$S_1$ transition in the spectral range between 365–435 nm and the resulting series of fluorescence features range from 435–550 nm (see Experimental Section). Specifically, two of the distinct emission peaks are observed around 450 nm and 480 nm; as previously reported, the ratio of the amplitude of the 480 nm peak to that of the trough between the adjacent peaks (occurring at ≈465 nm) can be utilized as a quantitative measure of temperature.[42] The linear ratio change with temperature is due to an enhancement in the non-radiative decay rate which asymmetrically affects the relevant emission pathways, dependent on both the intrinsic photo-physical properties of the fluorophore[43] and the extrinsic polymer relaxation processes.[44,45] The utilization of an emission amplitude ratio makes this approach robust to fluctuations in excitation laser intensity, local variations in dye molecule concentration, or temperature-induced shape changes of the emission bands.

We point out that the temperature reported in this manner will be an average of signals from the ensemble of fluorescing molecules; that is, dye molecules located nearer to a metal nanoparticle will experience a higher local temperature than those situated far from a nanoparticle. Due to the dilute concentrations of both perylene and gold nanoparticles, most fluorophores will predominantly be far from the nanoparticle heaters and the observed temperature will be an average over the polymer matrix.
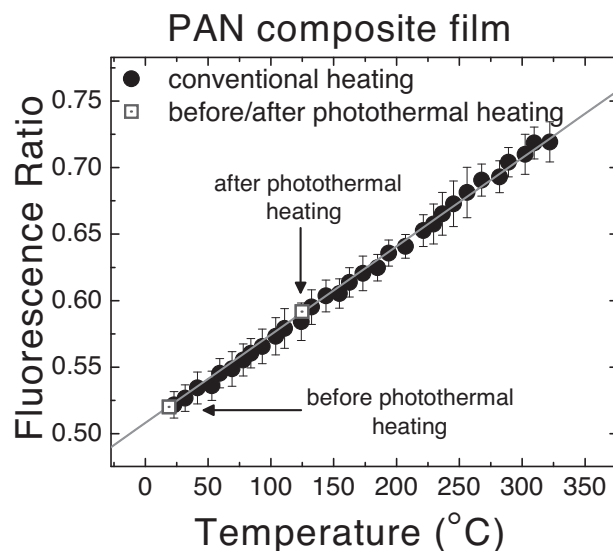


**Figure 1.** Temperature measurement of a PAN composite film after conventional (filled circles) and plasmon-mediated (open squares) heating using the perylene fluorescence ratio technique. Conventional heating allows calibration of the fluorescence-temperature relationship: measurement of the trough-to-peak ratio during photothermal heating enables active temperature measurement. The line is a linear fit to the measured data points from conventional heating.

**Figure 1** (filled circles) shows a temperature calibration curve for perylene doped in a poly(acrylonitrile) (PAN) thin film composite (9.84 ± 1.50 μm thick, containing 0.02% volume fraction of perylene and 0.15% volume fraction of ≈25 nm diameter gold nanoparticles) where the sample is conventionally heated using a computer-controlled stage and the perylene fluorescence emission ratio of the "trough" (465 nm) to the "peak" (479 nm) is measured. Subsequently, using this experimentally determined relationship, observations of the fluorescence ratio value can then be directly correlated with a polymer sample's average temperature when it is altered by non-traditional heating mechanisms. In particular, as indicated in Figure 1, the temperature T of this PAN composite sample increased from ≈20 °C (i.e., from $T_i$ = the initial ambient laboratory temperature) to 124.6 ± 0.7 °C after 20 minutes of irradiation by the green laser (0.10 W/cm² at 532 nm).

Thus, a thin composite film can be efficaciously heated by the photothermal effect via irradiation with green light approximately spectrally coincident with the SPR maximum of the embedded gold nanoparticles (see Experimental Section): the inferred average temperature rise (here due solely to the plasmon-mediated mechanism) is optically measured by the perylene emission ratio (open squares in Figure 1). As discussed later, this remote, non-destructive measurement of the temperature enables study of the dominant heating and cooling rates in the system, and how these rates change with sample temperature, sample morphology, and nanoparticle concentration; thus, both the process of coming to equilibrium and the final equilibrium temperature attained can be readily observed.

The accuracy of this fluorescence-based thermometer is verified utilizing a sample that undergoes a permanent morphological

change upon sufficient heating. For a given polymeric material, the measured fluorescence ratio calibration curve is identical for both film and nanofibrous mat samples; however, heat-induced irreversible shape changes in samples containing nanofibers can be observed via scanning electron microscopy (SEM) images. Because nanofibrous samples have distinct morphology, the effect of melting can be clearly demonstrated. In particular, nanofibrous mat samples consist of a planar collection of ≈250 nm diameter cylindrical nanofibers fabricated by electrospinning, arranged randomly with a porosity of ≈70%. PAN has a glass transition temperature ($T_g$) of 125 °C and a melting temperature ($T_m$) of 326 °C. Under the photothermal heating induced by the green light (532 nm at 0.10 W/cm$^2$), PAN nanofibrous mats reach T = ≈125 °C; at this temperature the nanofibers exhibit slight relaxation and occasional fiber breakages (similar to previously observations[41] of nanofibrous mats annealed at temperatures below $T_m$) but this thermal change is not sufficient to generate any dramatic morphological alterations (data not shown).

However, if a different polymer system (poly(ethylene oxide) (PEO): $T_g$ = –65 °C and $T_m$ = 66 °C) is utilized, permanent temperature-induced morphological changes can be observed. **Figure 2** summarizes experiments showing calibrated fluorescence ratio versus temperature data (filled circles) for a composite PEO film step-wise heated using the computer-controlled stage. In a PEO nanofibrous mat sample (10.58 ± 2.09 μm thickness, containing 0.02% volume fraction of perylene and 0.15% volume fraction of ≈25 nm diameter gold nanoparticles) a temperature T = 67.1 ± 0.6 °C is attained after photothermal heating for 20 minutes. SEM images for different temperature points
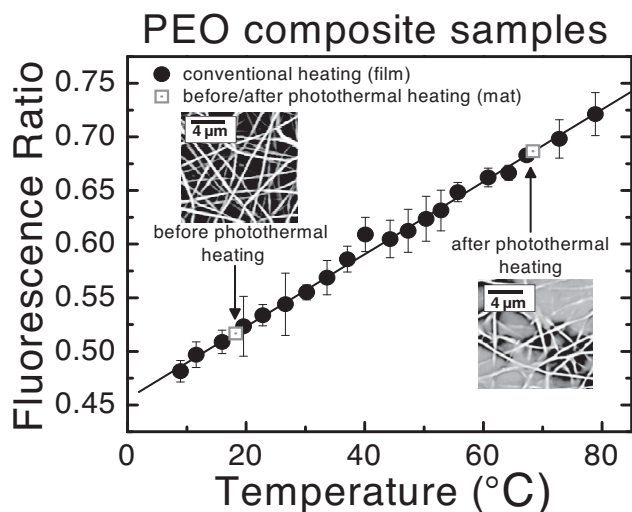


**Figure 2.** Morphological changes under heating for a PEO composite film sample. The fluorescence ratio data (filled circles) measured when conventionally heating a film sample using the computer-controlled stage is used to calibrate the temperatures reached in a mat sample under photothermal heating (open grey squares). The SEM images compares the morphology of PEO nanofibrous mats under the plasmonic-heating before (upper left inset) and after (lower right inset) reaching the polymer melting point. The line is a linear fit to the measured data points from conventional heating.

along the heating curve correlate with the optically measured temperatures, confirming fiber relaxation and merging followed by the loss of defined structure as $T_m$ is reached for this polymer. The inset images in Figure 2 depict the mat sample at two representative points (open grey squares) of the initial ambient temperature and after being photothermally heated to ≈$T_m$. These results are consistent with a previous study of photothermal heating of PEO nanofibrous samples where SEM analysis was used to definitively demonstrate that the morphological changes to the mats (pre-melting and melting) were due to the presence of nanoparticles and irradiation with light resonant with the nanoparticle SPR.[41]

Thus, implementation of the fluorescence thermometry technique enables monitoring of the internal sample temperature without necessitating destructive shape changes due to melting to determine the temperature. Additionally, this measurement approach allows samples having non-distinct morphological features to be utilized to explore the limits of photothermal heating, such as thin films (i.e., materials with smooth, continuous features), as well as such samples composed of polymers which possess significantly higher $T_m$ (i.e., which might not be attained under the given excitation intensity).

## 2.2. Effect of Increasing Laser Intensity for Different Sample Morphology and Environment

With an established capability to remotely measure the sample temperature, variation in photothermal heating due to irradiation intensity, nanoparticle concentration, polymer type, and sample morphology can be directly observed in real-time and, by determining the rate of the temperature change, both the initial response and equilibrium behavior can be studied. **Figure 3** shows the temperature increase ($T_0$) above the initial room temperature ($T_i$) for PAN samples after a steady-state temperature ($T_{SS}$) is achieved under different excitation laser intensities (i.e., $T_{SS} = T_i + T_0$). For a ≈10 μm thick nanocomposite film at ambient (Figure 3a, filled squares), as the green light intensity is increased, the maximum temperature achieved increases at a roughly linear rate for low intensities (<0.10 W/cm$^2$, up to a temperature gain of $T_0$ ≈ 105 °C), as seen more clearly in the inset which is an expanded view of the graph. At higher laser intensity and higher temperatures (above $T_0$ ≈ 125 °C) a second linear relationship with lower slope is observed. Between these two regions, a transition is observed, which begins at approximately the PAN bulk $T_g$. This result is caused by the fact that in this temperature range (i.e., T > $T_g$), the photothermally deposited energy can couple to the cooperative segmental motions now available. Naively, thinking of these experiments in a simple calorimetric format: $q_{in} - q_{out} = mc\Delta T$, ($q_{in}$ is the heat input to the sample from photothermal heating, $q_{out}$ is the heat loss, $m$ is effective mass, $c$ is the material specific heat, and $\Delta T$ is the resultant temperature increase), and the specific heat of the material undergoes a change above $T_g$.

Ultimately, PAN composite films attain $T_0$ = 164.9 ± 9.4 °C (170.4 ± 2.9 °C) at the highest laser intensity utilized (3.6 W/cm$^2$) (Figure 3a) under ambient conditions (in vacuum). $T_0$ ultimately reflects the balance between the heat introduced by the photothermal heating and the various heat loss

**ADVANCED
FUNCTIONAL
MATERIALS**
www.afm-journal.de
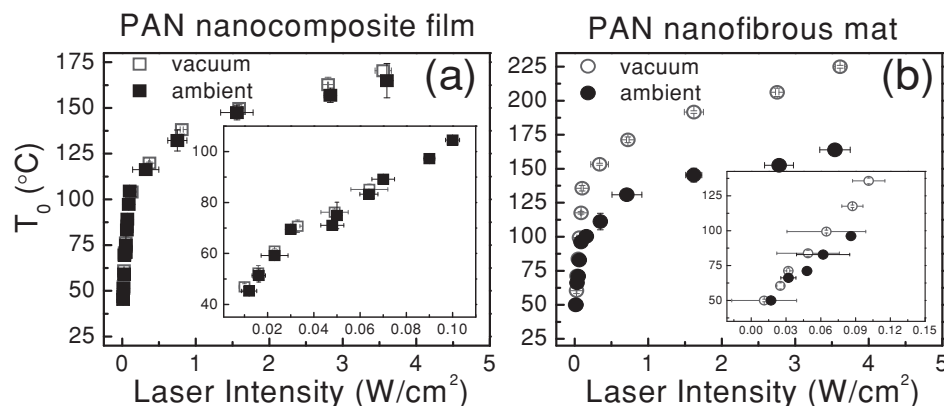
FULL PAPER

*Materials Views*
www.MaterialsViews.com

**Figure 3.** Temperature change attained at steady-state in a polymer nanocomposite material via the photothermal effect of gold nanoparticles (2.5 wt% having ≈25 nm diameters) embedded in PAN for different sample morphology. a) ≈10 μm thick PAN nanocomposite film. A maximum increase of $T_0 = 164.9 \pm 9.4$ °C (170.4 $\pm$ 2.9 °C) was reached under ambient (vacuum) conditions with an illumination intensity of 3.6 W/cm². The inset is an expanded view of the quasi-linear region (up to $T_0 \approx 105$ °C at 0.10 W/cm²). b) ≈10 μm thick PAN nanofibrous mat. A maximum increase of $T_0 = 164 \pm 3$ °C (225 $\pm$ 1°C) was reached under ambient (vacuum) conditions with an illumination intensity of 3.6 W/cm². The inset is an expanded view of the quasi-linear region, up to $T_0 \approx 100$ °C under ambient conditions ($T_0 \approx 135$ °C in vacuum) at 0.10 W/cm². Note: the bulk value of $T_g = 125$ °C which is equivalent to $T_0 \approx 105$ °C.

mechanisms. In order to probe the relative importance of convection, conduction, and radiation, both sample morphology and the surrounding environment can be modified. For instance, the open squares in Figure 3a show the temperature increase when the sample is placed in vacuum (≈10⁻⁷ torr), where the cooling process of convection is effectively eliminated. The relatively small difference between the final temperatures achieved under the two environmental conditions suggests that for the film morphology, the most impactful energy loss mechanisms are thermal conduction to the underlying glass substrate and radiation to the environment (which should be a minimal, secondary loss except at the highest temperatures).

Figure 3b depicts corresponding observations for a similarly thick (≈10 μm) nanofibrous mat, where a maximum $T_0 = 164 \pm 3$ °C (225 $\pm$ 1 °C) is attained at 3.6 W/cm² excitation intensity under ambient conditions (in vacuum). At the lower applied intensities, there is also a comparable linear increase in sample temperature under both environmental conditions until $T_0 \approx 100$ °C is reached, above which the photothermally driven temperatures diverge. The mat sample in ambient mimics the behavior of the film sample, correspondingly raising its temperature with a reduced slope; however, in vacuum, the sample continually increases with the higher excitation intensity at the original rate until $T_0 \approx 135$ °C is achieved before additional temperature increase but with a reduced positive slope.

Such sample thermal behavior can intuitively be understood by considering the available cooling mechanisms of radiation, conduction, and convection. In general, radiation losses will always be present independent of sample morphology as the temperature of a substance exceeds the environmental $T_i$, but this pathway will only weakly influence the heating dynamics until a large thermal differential (≈100–200 K) relative to the ambient environment is established. Now considering sample shapes and structures, for films, the process of convection will primarily occur only along the topmost surface of the sample; therefore, heat conduction through the film to the underlying

substrate is typically the most significant cooling mechanism with, depending upon the temperature differential with the environment attained, radiation losses also contributing. For mat samples having nanofibrous morphology, owing to their high intrinsic porosity, the thermal mass is greatly reduced and the sample is largely comprised of void space, possessing significantly increased surface area (≈3×) over a similarly sized film sample. Due to this enhanced surface area, convective processes must strongly influence such samples' thermal behavior, therefore eliminating this mode of heat loss by placing the sample in vacuum as expected results in the sample reaching a higher temperature for the same given laser excitation intensity. While still present, heat loss from conduction is greatly reduced in a mat sample due to its morphological structure: for the layers of fibers comprising the sample, heat can conduct along the polymeric nanofiber but only transport to adjacent layers of the sample through the intermittent fiber-to-fiber contact locations. This geometry effectively makes the characteristic path length for conduction of the thermal energy to reach the substrate dramatically longer than the physical thickness of the mat sample; furthermore, the small fiber cross-section and high thermal resistance of the fiber-fiber contacts additionally act to inhibit conductive heat flow. Subsequently, the dramatic enhancement in the sample temperature attained for a mat under fixed light intensity in a vacuum versus ambient conditions is an understandable consequence of the elimination of the dominant convective losses.

## 2.3. Effect of Changing Nanoparticle Concentration

For a given fixed excitation light intensity, there is also a proportional increase in steady-state temperature $T_0$ for samples with higher concentrations of nanoparticles; simply put, more available local heaters result in a greater temperature increase. **Figure 4** depicts the steady-state temperature attained above

www.MaterialsViews.com

ADVANCED
FUNCTIONAL
MATERIALS
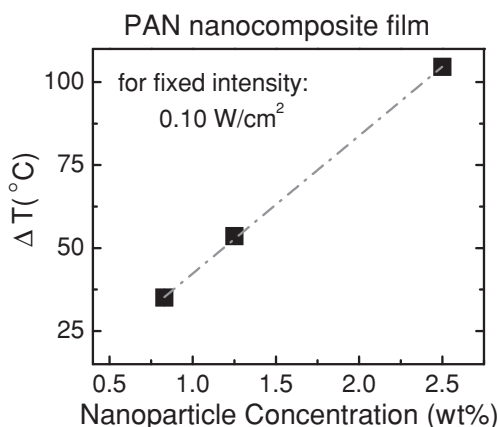www.afm-journal.de

FULL PAPER

**Figure 4.** Steady-state temperature versus nanoparticle concentration for PAN films in ambient. The steady-state temperature ($T_0$) reached above ambient at a fixed 0.10 W/cm² excitation intensity linearly scales as the concentration of the nanoparticles in the samples is increased.
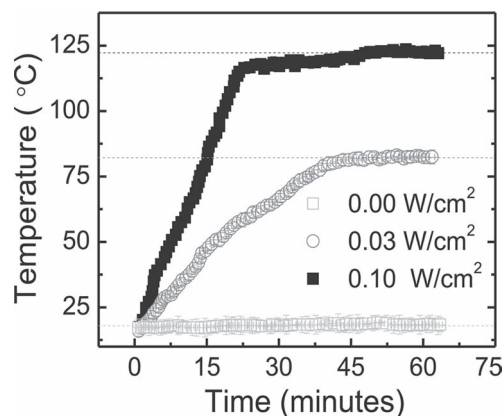


**Figure 5.** Temperature (T) attained as a function of time when varying the 532 nm laser intensity for PAN nanocomposite films in ambient. For comparison, temperature measurement with no green light present (open light grey squares) is also shown. The attained steady-state temperatures are indicated by a horizontal dotted line: grey (black) for 0.03 W/cm² (0.10 W/cm²) where $T = 82.8 \pm 0.5$ °C ($T = 122.2 \pm 0.7$ °C), respectively. The ambient temperature $T_i = 18$ °C is indicated by the light grey horizontal dotted line.

ambient of three ≈10 μm thick PAN film samples with varying amounts of the gold nanoparticles where the dashed line is a linear fit to the data. For well-dispersed samples, increasing the number of nanoscale heaters will proportionally raise $T_0$ until the inter-nanoparticle spacing becomes small enough[38] (i.e., d < 5r, where d(r) is the nanoparticle spacing (radius), respectively) to influence the nanoparticle's SPR[46] and decrease the efficacy of the photothermal effect.[41] Note, in general unless otherwise indicated in this report, the laser intensity used is 0.10 W/cm² and the gold nanoparticle's concentration of the samples is 2.5 wt%, sufficiently dilute to provide well-separated nanoscale heaters.

## 2.4. Observing Time-Dependence of Heating in Nanocomposite Samples

This thermal measurement technique also enables observation of how the temperature equilibrium is reached under different photothermal driving conditions. For example, **Figure 5** depicts the change in temperature with time of a PAN nanocomposite film when irradiated with two different laser intensities in ambient conditions. As expected, lower intensity irradiation (Figure 5: 0.03 W/cm², open grey circles) results in a reduced final equilibrium temperature ($T = 72.8 \pm 0.5$ °C) as compared to that attained with a higher excitation intensity ($T = 122.2 \pm 0.7$ °C) (Figure 5: 0.10 W/cm², filled squares). For comparison, data points are also shown that demonstrate that the sample temperature remains constant when the green light is absent ($T =$ ambient temperature $T_i = 18$ °C) (Figure 5: 0.00 W/cm², open light grey squares).

In the temperature versus time curves, the rate at which equilibrium is reached is dependent on the loss rate due to all cooling mechanisms present, which for these samples and temperature range is dominated by convection and conduction. As revealed in Figure 5, at the higher sample temperatures attained at increased laser intensity, the losses are also enhanced, and the system comes to equilibrium more quickly (after ≈25 min)

as compared to under the lower laser intensity (after ≈39 min). We further analyze and discuss the shape and details of the heating curves below.

We point out that the dye molecules do not absorb at 532 nm (see Experimental Section) and when the sample is solely excited by the weak 405 nm laser, no heating is observed (Figure 5); hence the perylene acts solely as a temperature reporter. These experiments thus demonstrate unequivocally that the heating observed is due to the photothermal response of the nanoparticles and that substantial temperature increase can be accomplished even within solid non-fibrous samples. This facile ability to remotely control the internal application of heat in a polymeric material, while simultaneously monitoring its temperature, provides an extremely useful tool for material manipulation, processing, and characterization. We have successfully heated mats and films for three different polymers (PAN, PEO and poly(methyl methacrylate) (PMMA)) utilizing the photothermal heating technique for a variety of different light intensities, both with, and without, the presence of forced convection. A variety of thicknesses were measured (10–40 μm), but we focus on samples with ≈10 μm thickness in this report. This range of experiments demonstrates the breadth of applicability of the technique.

## 2.4. A Simple Model to Understand the Important Factors Contributing to Sample Heating

**Figure 6** shows the time evolution of ≈10 μm thick PAN composite film temperature when irradiated with a laser intensity of 0.10 W/cm². If the overall sample system thermal response can be adequately described by a single temperature-independent heat loss rate (A), the temperature at any time is given by:
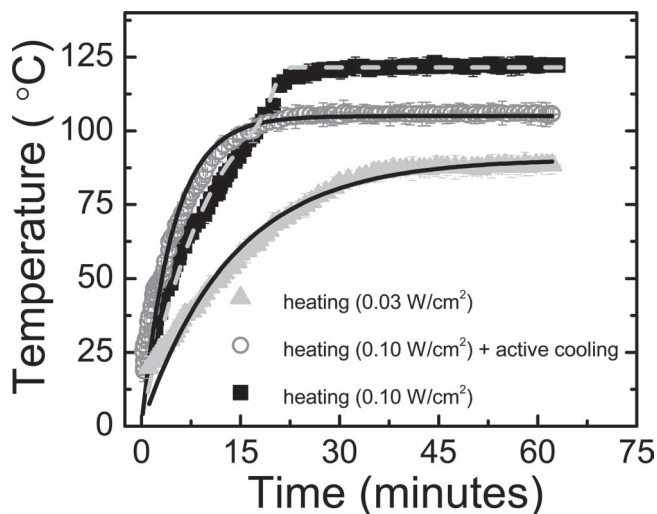
ADVANCED
FUNCTIONAL
MATERIALS
www.afm-journal.de

Materials
Views
www.MaterialsViews.com

**Figure 6.** The temperature versus time evolution of PAN composite films in ambient undergoing photothermal heating by embedded gold nanoparticles excited by a 532 nm green laser. At low excitation intensity (filled grey triangles, 0.03 W/cm$^2$) or higher intensity but with forced convection (0.10 W/cm$^2$, open grey circles), the measurement and single-exponential calculation (Equation (1); black lines) agree reasonably well. Under ambient conditions and higher intensity (0.10 W/cm$^2$, filled squares), where temperature-dependent effects are manifested as time-dependent changes, the data and calculation (dashed grey line) agree only when a varying $A$-value is used.

$$T = T_i + T_o[1 - \exp(-At)] \tag{1}$$

where $T$ is the temperature at time $t$, $T_0$ is the maximum steady-state temperature attained above the initial value (determined by the ratio of the heating and cooling rates), and $T_i$ is the initial temperature (i.e., the ambient temperature of the environment). Thus $q_{out}$, the heat loss per time, is determined by three contributions as: $q_{out} = kS(T - T_i) + \frac{k^* A^*}{l}(T - T_i) + \sigma \varepsilon S(T^4 - T_i^4)$, where $k$ is the convective heat transfer coefficient (which depends upon the composition and velocity of the surrounding air), $S$ is the surface area, $k^*$ is the thermal conductivity of the medium (i.e., the polymer matrix), $A^*$ is the cross-sectional area for conduction, $l$ is the characteristic length for conduction (e.g., for samples with film morphology, the thickness), $\sigma$ is the Stefan-Boltzmann constant, and $\varepsilon$ is the emissivity of the sample material. Under the experimental conditions discussed in detail here (i.e., the given dilute nanoparticle concentration and low intensity laser radiation), convection and conduction are the dominant mechanisms to consider; thus, dropping the radiation terms and combining gives the expression: $A = \frac{kS + (k^* A^* / l)}{mc}$, where $m$ is a characteristic mass and $c$ is the specific heat of the material. The heating rate B is defined as $B = \frac{q_{in}}{mc}$. Setting $q_{in} - q_{out} = mc(T - T_i)$ and solving the resultant differential expression yields Equation (1), where $T_0 = \frac{B}{A}$.

The above model treats the heating rate as a simple bulk quantity; this assumption is similar to the experimental measurement of the sample, as the observed temperature is an average result due to contributions from many nanoscale heaters located at a distribution of distances away from the ensemble of sensing fluorophores homogeneously distributed

throughout the sample. Consequently, Equation (1) is useful for understanding the problem and may be sufficient for some experimental realizations. However, we note that the simple expression is not fully appropriate for direct comparison to the measured outcome under all cases due to several temperature-dependent effects. First, when heating under ambient conditions, air in the boundary layer surrounding the sample warms up; thus, the convective heat transfer coefficient $k$ changes with sample temperature. Second, the thermal conductivity $k^*$ of the polymer matrix likely has an intrinsic, relatively weak temperature dependence, which can usually be ignored if the induced thermal change is not substantial, however, due to the efficacious nature of the photothermal effect employed here, large temperatures changes are possible and thus, this effect must often be considered. Finally, as discussed above, if the sample temperature surpasses $T_g$ for the specific polymer, $k^*$ of the medium is altered and the related property of heat capacity of the material is also changed. Thus, the presence of all these contributions to the overall heat loss $A$ can result in notable time-dependence under certain measurement conditions. For those cases, however, we find reasonable fits from the basic model to the experimental data are still obtained by utilizing a non-constant (i.e., sigmoidal) value for the overall cooling rate $A$.

Figure 6 depicts measured photothermal heating curves for a PAN composite film embedded with gold nanoparticles (2.5 wt% gold nanoparticles) under different green laser illumination intensities and cooling conditions. For low excitation intensity (filled grey triangles, 0.03 W/cm$^2$) or higher intensity under conditions of forced convection created by directing room temperature air onto the sample using a small fan (open grey circles, 0.10 W/cm$^2$), the steady-state temperatures reached (88.6 ± 0.4 °C and 106.2 ± 0.3 °C, respectively) stay sufficiently below $T_g$ such that a single-value for $A$ is adequate for reasonable agreement between the model (black lines) and experimental results. Under these conditions, the temperature change is sufficiently small (low intensity) or the enhanced cooling rate $A$ is more temperature (and time) independent (with forced convection present) and the final temperature attained below $T_g$, so $k^*$ is less variable over this observed sample temperature range. In contrast, for the higher intensity excitation under ambient conditions (filled squares, 0.10 W/cm$^2$), a temperature of 121.6 ± 0.5 °C was reached, and a time-varying $A$ required to achieve good simulation (dashed grey line) and experimental data agreement. As is further evident in the figure, the achieved steady-state temperature increase ($T_0$) under conditions of forced convection was lower, and the sample equilibrated faster, as compared to same excitation intensity ambient conditions. This observation is consistent with the theoretical discussion above: that is, while the heating rate ($B$) is unaffected by the fan application, the cooling rate ($A$) is larger, leading to a lower $T_0 \sim \frac{B}{A}$ and a correspondingly faster approach to equilibrium (driven by $A$).

Utilizing this theoretical approach also enables further understanding of the previously observed behavior in $T_0$ with light intensity (Figure 3a) and nanoparticle concentration (Figure 4). Rewriting earlier expressions for convenience as: $T_0 = \frac{q_{in}}{(kS + \frac{k^* A^*}{l})}$, we also point out that $q_{in}$ must be proportional to the excitation light intensity (i.e., the fluence of photons which are resonant with the SPR of the metal nanoparticles) and the

Materials
Views

www.MaterialsViews.com

ADVANCED
FUNCTIONAL
MATERIALS
www.afm-journal.de

FULL PAPER

nanoparticle concentration (i.e., the number of independent nanoscale heaters within the sample to generate the localized heating). In particular, assuming a homogeneous spatial distribution of nanoparticles, after a resonant photon is absorbed by an individual nanoparticle, the plasmon typically relaxes in a few $\approx 10^{-12}$ s, much faster than the average time between available excitations (e.g., $\approx 10^{-7}$ s for an excitation intensity of 0.10 W/cm$^2$ and the appropriate absorption cross-section for gold nanoparticles)[8] indicating that the metal nanoparticle thermal response will be linear with laser intensity for all cases in this report. Further, for a given sample, the surface area $S$, cross-sectional area $A^*$, and conduction length $l$ should all be approximately constant, thus the observed onset of non-linearity of the steady-state temperature $T_0$ versus excitation light intensity curve in Figure 3a reveals the impact of changing contributions from the convection ($k$) and conduction ($k^*$) terms as the sample temperature rises significantly above the ambient temperature. In particular, the slope of the curve begins to noticeably roll over and flatten above $T_g$, reflecting the above-mentioned effects and contribution from the changing material specific heat value, whereas in contrast, in the temperature range below $T_g$, there is a predictable, highly linear change in sample temperature for change in excitation intensity. Similarly, for the fixed excitation intensity and well-dispersed nanoparticles, a purely linear increase in temperature attained above ambient as nanoparticle concentration is raised (Figure 4) is consistent with the above discussion, as the final sample temperature remains below $T_g$.

**Figure 7** reveals measurements of temperature versus time for PAN, PMMA and PEO films under two different excitation laser intensities. The PAN ($T_g$ = 125 °C; $T_m$ = 326 °C) and PMMA ($T_g$ = 120 °C) samples reach similar temperatures ($\approx 90$ °C under 0.03 W/cm$^2$ and $\approx 120$°C under 0.10 W/cm$^2$, respectively) for the same given excitation light intensity. In contrast, under these same irradiation conditions, PEO ($T_g$ = −65 °C; $T_m$ = 68.4 °C) attains only $\approx 45$ °C and a maximum of $\approx 68$ °C, which is its melting point.

These observed variations in steady-temperatures achieved under the same photothermal heating conditions (i.e., nanoparticle concentration and excitation light intensity) for similarly sized samples reflect the intrinsic differences in physical characteristics between the polymer matrices. First, consider the experimental curves (Figure 7, the filled square, triangle, and circle data points) generated under the higher excitation intensity (0.10 W/cm$^2$ at 532 nm). Figures 1 and 2 previously demonstrated that the perylene thermometer still functions through the glass and melting phase transitions and to temperatures well above $T_m$. Clearly, when a polymeric sample is photothermally heated to $T_m$ and begins melting (or becomes molten), significant new loss mechanisms (including the latent heat of melting and convection of the liquid polymer) are introduced to the system, which make temperature increases more energetically burdensome. Hence, for PEO (Figure 7, top graph), the photothermal effect of the nanoparticles under the given laser intensity is sufficient to melt the sample but not robust enough to raise the temperature further. The fact that the temperature remains constant with the given laser intensity reflects a balance between the heating and cooling rates, indicating that the nanoparticles are still functioning as photothermal heaters and
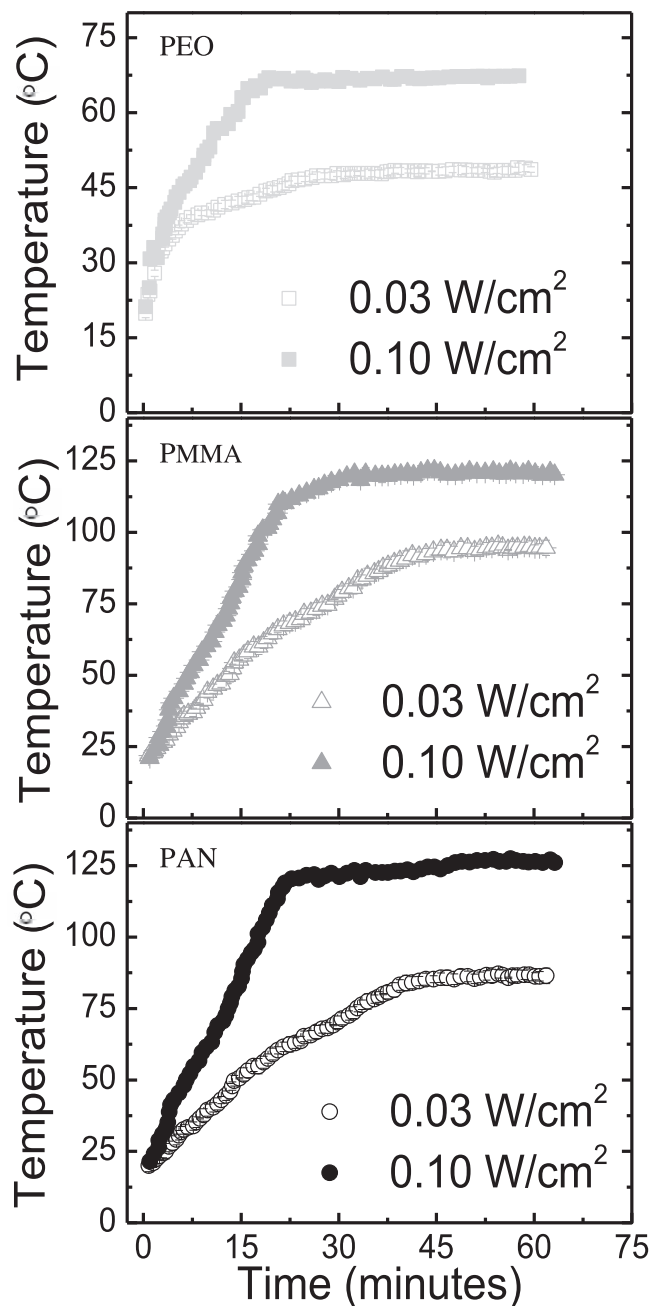


**Figure 7.** Measured temperature versus time for three different composite polymer film samples, doped with the same volume fraction of nanoparticles and under identical illumination conditions in ambient.

have not been damaged or undergone agglomeration in the melt. Therefore, significantly increased laser intensity would be subsequently required to additionally raise the temperature of the molten PEO material. For the PMMA and PAN samples (Figure 7, middle and lower graphs, respectively), the equivalent temperature reached reflects the similar thermal characteristics of the polymers and higher values for $T_g$. The lower excitation intensity (0.03 W/cm$^2$ at 532 nm) data curves (Figure 7, the open circle, triangle, and square data points) reveal a similar
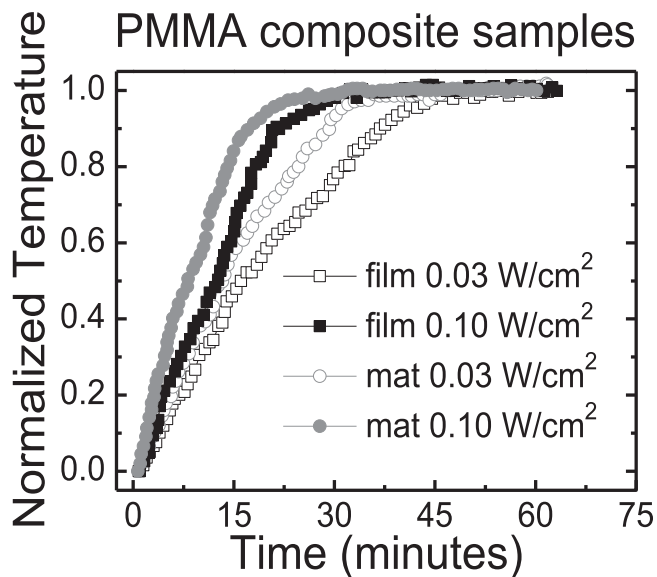
## PMMA composite samples



**Figure 8.** Normalized temperature versus time curves for two different laser excitation intensities and sample morphologies in ambient. For both morphologies [films (squares symbols) and mats (circle symbols)], the steady-state temperature is attained faster for the higher laser intensity (solid symbols) because of a larger heat loss $A$ due to higher sample temperature (resulting from the larger driving rate $B$) which approaches $T_g$ at long times. Comparing morphology, the steady-state temperature is reached more rapidly for mats versus films, due to larger convective losses (i.e., higher $A$) from the larger surface area. All samples were ≈10 μm thick.

trend. Under identical heating conditions, PEO reaches a lower temperature than similarly doped polymer samples of PMMA and PAN. This is understood because for PAN and PMMA samples, the temperature remains well-below their respective $T_g$ values but for PEO, the sample temperature is in the range $T_g < T < T_m$.

### 2.5. Effect of Sample Morphology Revealed from the Simple Model Cooling Rates

Naturally, cooling rates are also influenced by the morphology of sample. In **Figure 8**, heating of a nanofibrous mat of PMMA is compared with a film of the same thickness and nanoparticle concentration for two different excitation laser intensities under ambient conditions. In order to focus the discussion on the rate of temperature change for the experiments, each curve in the figure has been normalized to the attained final temperature. Clearly, it is expected that increasing the excitation intensity raises the ultimate steady-state temperature reached by the sample (see Figure 7) because it increases the heating rate $B$, as discussed previously. Examining the film data (square symbols) in Figure 8 reveals that there is also an increase in the value of $A$ as the excitation light intensity is raised (open versus filled symbols), manifested by a reduction in the time required to reach the temperature equilibrium; thus confirming the prior discussion of the temperature-dependent heat loss parameters.

Hence, for films in Figure 8 both $A$ and $B$ values are larger with higher excitation intensity, but the relative change in B is greater. Note: if the relative changes in $A$ and $B$ were equivalent, then the final temperature attained above ambient ($T_0$) would remain unchanged; see below. The same trend is shown for the nanofibrous mats (Figure 8, circle symbols). However comparing mats and films under identical heating conditions, the loss rate $A$ in mats (as revealed from the slope of the normalized temperature versus time graph in Figure 8) is found to be always higher (by a factor of ≈1.3×) than in a film sample of comparable thickness. In this circumstance, the enrichment in the relative $A$ value is due to the enhanced surface area present in the mat sample; the fibrous morphology provides ≈1.2× increase in the surface area for each layer versus the entire film sample. Overall, ignoring fiber-fiber contacts, the mat morphology possesses ≈50× the surface area versus a film (e.g., comparing ≈10 μm thick samples). These experimental results suggest that the topmost few layers have the most significant effect in providing the convective thermal loss for mats. Given the fact that under ambient conditions there is no explicit driving force for air to penetrate into the sample, even with ≈70% porosity, it is reasonable that air flow is limited in the sample interior.

Interestingly, despite the enhanced cooling rate when transitioning to a nanofibrous structure, the experimentally observed steady-state temperatures (Figure 4a and b) (below the polymer $T_g$) under identical excitation light intensity and ambient conditions were relatively robust to changes in sample morphology (i.e., film versus nanofibrous mats) because any changes to $A$ and $B$ tended to be correlated. The nanofibrous morphology not only enhances convective loss (due to higher surface area) but also scattering of the excitation light, which paradoxically increases the heating rate. Essentially, any scattering of 532 nm light which occurs below the top few layers of the nanofibers redirects the light within the sample, increasing the possibility of the photons being absorbed by the embedded nanoparticles in the mat samples, rather than being lost. The result of this scattering effect is as if an increased light intensity was used to illuminate the sample (or, as if the effective light path length through the sample was longer, allowing for enhanced absorption by the material)[47] and raises $B$ for nanofibrous samples, partially offsetting increases in $A$. Since these two effects both simultaneously arise from the presence of the sample's nanofibrous morphology, they correlate and thus, $T_0$ is relatively constant under natural convection conditions. Supporting this interpretation, a study comparing photobleaching rates of the perylene in films and mats is presented as Supporting Information.

### 2.6. Enhancement of Photothermal Heating Due to Morphology-Dependent Light Scattering

In any optically driven experiment probing the interior of a material, the irradiation intensity as a function of sample depth depends on the processes of absorption and scattering which occur along the light path. To better understand the intensity versus depth profile within the nanocomposite materials used in these experiments at the two different spectral wavelengths

**Table 1.** Penetration depth in different morphological nanocomposite samples at the excitation wavelengths for the photothermal heating (532 nm) and the temperature fluorescence probe (405 nm) lasers.

| Nanocomposite sample morphology | 532 nm penetration depth $d_o$ [μm] (2.5 wt% gold nanoparticles) | 532 nm penetration depth $d_o$ [μm] (1.25 wt% gold nanoparticles) | 405 nm penetration depth $d_o$ [μm] (0.009 wt% perylene) |
|---|---|---|---|
| mat | 11.64 | 26.84 | 13.29 |
| film | 6.76 | 11.62 | 7.73 |

(the photothermal heating laser for the gold nanoparticles at 532 nm and the optical probe of perylene at 405 nm), ultraviolet-visible extinction measurements were taken for samples of differing thickness and morphology (data not shown). Curves of the percent transmittance $T$ versus sample thickness $d$ are well-fit by the single decaying exponential form: $T = 100\left(e^{-\frac{d}{d_o}}\right)$, where we refer to $d_o$ as the penetration depth parameter. From data in **Table 1**, the $d_o$ values were similar for each of the two excitation wavelengths (i.e., 405 nm and 532 nm), revealing that combined effects of the given concentration and absorption cross-sections for the fluorophores and nanoparticles were similar: thus, the fluorescence temperature measurement and the photothermal heating effect influenced/probed similar volumes within the material. However, the penetration values varied significantly (≈2×) between nanofibrous samples and solid films. A second experiment utilizing a sample fabricated with one-half the nanoparticle concentration confirmed this observation; as expected, when the nanoparticle concentration is halved, the penetration depths roughly double as twice as much composite material is required to contain the same number of absorbers. Comparing the results from nanofibrous and solid film samples, taking into account the 70% porosity of the mats–and thus a smaller nanoparticle density per sample volume, if only considering the contribution from absorption (proportional to particle concentration), then the expectation is that the penetration depth of a mat would scale to ≈3× larger than that of the film. However, the penetration depth only increases by a factor of ≈2× because the nanofibrous morphology (i.e., fibers with diameters on the order of the wavelength of light) enhances scattering, as compared to the relatively smooth surface of the amorphous films. Thus, the absorbance is ultimately more efficient in the mats, due to the opportunity for photons to scatter and be absorbed rather than pass through the sample. This enhanced absorbance decreases the effective penetration depth.

## 3. Conclusions

The application of low intensity, resonant light to excite the surface plasmon resonance of metal nanoparticles and thereby, photothermally heat the surrounding material has been utilized in both nanofibrous materials with complex morphology and nanocomposite films composed of different polymer matrixes in order to thermally process the material. The challenge of temperature-sensing in nanoscale materials can be overcome by employing fluorescent probes as temperature sensors. By fabricating a polymer composite in which the fluorophores are in proximity of the nanoparticles, the temperature change in the polymer matrix can be tracked by studying the change in

fluorescence spectrum of the fluorescing molecules. The efficacy of the technique was demonstrated in both nanofibrous mats and film samples: for similarly thick samples, temperature increases on the order of ≈100s °C are easily obtained with relatively low irradiation intensities. Control of the sample environment (i.e., ambient versus vacuum) can also be used to reduce heat losses and further enhanced the heating effect. A detailed analysis of resultant temperature as a function of material type (polymer and morphology), nanoparticle loading, resonant light intensity, surrounding environment and time was presented. As expected in any calorimetric process, the final temperature at a given laser irradiance depended strongly on the phase of the material (relative to $T_g$ and $T_m$). Such a detailed understanding of the photothermal process in solid materials enables use of this technique to selectively (time and spatial location specific) process, react, or cross-link materials in a solid state solely with application of relatively low intensity visible light.

## 4. Experimental Section

*Metal Nanoparticles*: The gold nanoparticles used in this study were synthesized using the Fren's method by the reduction of aqueous tetrachloroauric(III) acid with aqueous trisodium citrate solution [both Sigma Aldrich]. The citrate ions act as both reducing and capping agents. To additionally stabilize the nanoparticles, an equal amount of dry polyvinyl pyrrolidone (PVP) (Scientific Polymers Products, Inc.) to that of the tetrachloroauric acid was immediately added to the solution. All reagents were used without further purification.

The freshly prepared nanoparticle solution was drop-cast onto copper grids (Protochips CF-2/2-2C-25) coated with a 400 nm thick carbon layer having 2 μm holes and 2 μm spacing to determine the nanoparticle size distribution. Transmission electron microscopy (TEM) images were obtained using a Hitachi HF2000 transmission electron microscope (see inset, **Figure 9**). The nanoparticles were found to be roughly spherical in shape with an average diameter of 26 ± 6.9 nm. The location of the SPR of the nanoparticles in solutions (Figure 9) was measured with an ultraviolet–visible spectrometer (CARY 50 Scan).

*Polymer Composite Films*: Three different polymers, poly(ethylene oxide) (PEO), poly(methyl methacrylate) (PMMA) and poly(acrylonitrile) (PAN) were used in the study. PEO (molecular weight 900 000 g/mol) was dissolved in 2:1 water-ethanol mixture to obtain a 4 weight-percent (wt%) PEO solution (polymer:solvent ratio). PMMA (molecular weight 350 000 g/mol) was dissolved in 1:1 chloroform-dimethyl formamide mixture to obtain a 12 wt% PMMA solution; PAN (molecular weight 150 000 g/mol) was dissolved in dimethyl formamide (DMF) to obtain an 8 wt% PAN solution. The polymer composite solutions were prepared by mixing the polymer solutions with the aqueous nanoparticle solution, ultimately resulting in a 2.5 wt% (0.15% volume fraction) of nanoparticles in the final nanocomposite sample. Perylene powder (Sigma Aldrich # 394475-1G) was also added to the polymer-nanoparticle solutions; the mixture was magnetically stirred for 8–10 hours at room temperature to obtain 0.09 wt% (0.02% volume fraction) of perylene. The resultant suspension was then spin-cast (Laurell Technologies WS-650SZ-6NPP/
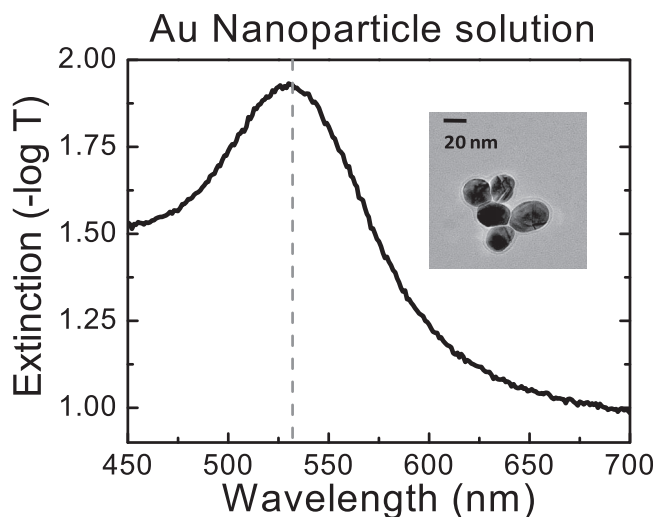
## Au Nanoparticle solution



**Figure 9.** Extinction spectrum of a solution of the gold nanoparticles, where the broad peak demonstrates the spectral location of the surface plasmon resonance (SPR). The vertical dashed line indicates how well the 532 nm laser matches the SPR for the 26 ± 6.9 nm diameter particles. Inset: TEM image of the nanoparticles.
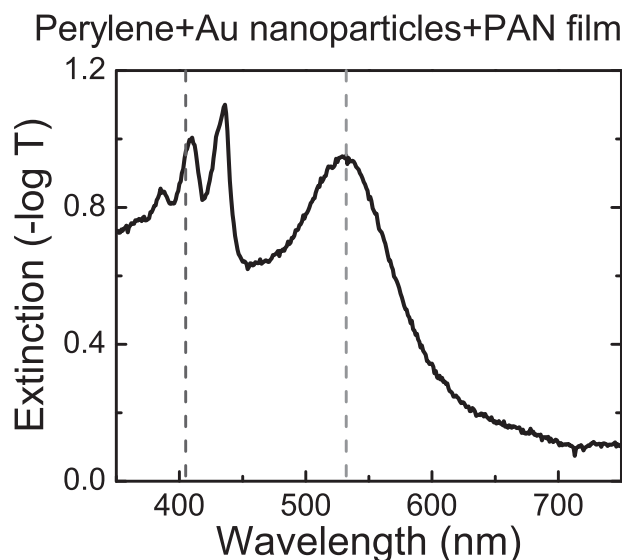
## Perylene+Au nanoparticles+PAN film



**Figure 11.** Extinction spectrum of a PAN composite film. The vertical dashed lines indicate spectral locations of the 405 nm (violet) and 532 nm (green) lasers, respectively.

lite) at 1500 revolutions per min onto 1 in × 1 in transparent slides (Fisherbrand, microscope cover glass 12-540B). The polymers (PEO, PMMA, and PAN) were initially dry (Sigma Aldrich); the solvents ethanol (Pharmco-AAPER), DMF (Fisher Scientific), and chloroform (Mallinckrodt Chemicals) were reagent grade and used without further purification.

The thickness of the resultant films was measured by an alpha step profilometer (Veeco Dektak Model 150). Measurements for the different polymer composite films confirmed that similar thicknesses were obtained: 9.5 ± 1.02 μm (9.84 ± 1.50 μm) for the PEO (PAN) composite films, and 10.82 ± 2.81 μm for the PMMA composite films. Comparison of extinction measurements of the individual perylene, nanoparticle, and polymer + perylene + nanoparticle solutions (**Figure 10**), and the polymer composite films (see **Figure 11** for PAN composite film) made using the ultraviolet-visible spectrometer reveals little or no spectral shifts between the metal nanoparticle's SPR in solution and solid phase, indicating that the relatively low concentration (2.5 wt% (0.15% volume fraction)) of nanoparticles within the final nanocomposite samples remains well-dispersed. There is no evidence of agglomeration within the material environment. The effect of particle agglomeration on photothermal heating is discussed in a previous publication.[41]

*Polymer Composite Nanofibrous Mat*: Nanofibrous composite mats are technologically useful materials for filtration,[27] tissue-scaffolding,[28] and energy applications[29] due to their high porosity and surface-to-volume ratios; much recent scientific effort has been made in developing new approaches[30] to increase the production rate of these types of nanomaterials. The polymer composite solutions were prepared in the same fashion as described above; nanofibrous mats were fabricated by traditional needle electrospinning of these same solutions. The electrospinning apparatus consisted of a programmable syringe pump (New Era Pump Systems, Model NE 500) and a positive polarity, high voltage power supply (Glassman High Voltage, Model No. FC60R2). Different polymer composite solutions were loaded into 10 mL syringes with a 4 in 20 gauge blunt tip needle. The tip-to-collector distance was 25 cm, and the applied voltage (needle-to-collector) was 15 kV. The pump operated at a feed rate of 5 μL/min for the PEO solution (20 μL/min for both PMMA and PAN solutions). Nanofibrous mats were collected directly onto 1 in × 1 in glass slides mounted onto an aluminum foil sheet covering the flat, grounded collector plate, by continuously electrospinning for 45 min.

Nanofibrous mats were characterized by analyzing images of the different polymer composite mats electrospun onto the glass
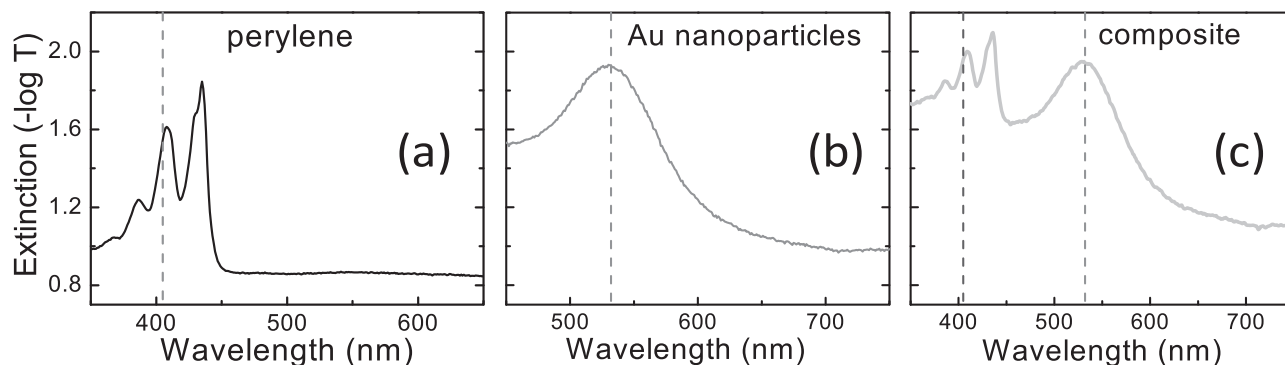


**Figure 10.** Comparisons of the extinction spectra of solutions of a) perylene; b) gold nanoparticles; and c) the perylene, gold nanoparticle, and PEO combination. Vertical dashed lines mark the spectral locations of the 405 nm (violet) and 532 nm (green) lasers, respectively.

www.MaterialsViews.com

ADVANCED
FUNCTIONAL
MATERIALS
www.afm-journal.de

FULL PAPER

substrates. The glass slides were attached to aluminum stubs and the samples sputter coated with Au/Pd in order to decrease charging. All images were obtained by scanning electron microscopy (SEM) (FEI Phenom-World BV) and then analyzed using ImageJ software. Images taken with 20,000x magnification were used to evaluate the size of the nanofibers; the fiber diameters were similar–264 ± 42 nm for PEO, 229 ± 32 nm for PMMA, and 251 ± 39 nm for PAN, as determined from >10 measurements on several different images. The porosity of nanofibrous mats was calculated by converting the image to grayscale and identifying the top most layer of the mat, then determining the relative number of marked (belonging to this first fiber layer) and unmarked pixels; typical mat porosity values were ≈70%. The thickness of mat samples were determined using the alpha step profilometer and similar for all three polymers: 10.58 ± 2.09 μm (9.13 ± 1.78 μm) for PEO (PAN) composite mat, and 10.21 ± 1.29 μm for PMMA composite mat.

*Non-Contact Temperature-Sensing Using Fluorescent Probes*: The polymer nanocomposites samples (i.e., thin films or nanofibrous mats) were mounted on a temperature-controlled stage. A 405 nm continuous-wave violet diode laser (operated at 5 mW power) expanded to a collimated ≈5 mm diameter spot size was used to excite the perylene molecules. This weak probe beam was flywheel-chopped at 2 kHz; a 50:50 beamsplitter allowed a portion of the beam to front illuminate the composite sample while the other portion, sampled by a photodiode coupled to a lock-in amplifier, monitored fluctuations in the laser amplitude. The perylene fluorescence was gathered and imaged (by serially oriented 50 mm diameter biconvex and 50 mm cylindrical lenses, both having focal lengths of 6 cm) onto the input slit of a double-grating scanning monochromator (SPEX 1680B), with the output signal detected by a side-on photomultiplier tube (PMT) detector (Hamamatsu 931B) operated at −800 V. A 435 nm dielectric low pass interference filter (Omega Optical) was used to block any scattered light from the violet laser; a short pass dichroic beamsplitter (CVI) rejected reflected 532 nm light from the green laser. Overall measurement system spectral resolution was ≈1 nm. The amplified PMT output was photon-counted (Stanford Research Systems SR400), with a corresponding background subtraction from equal counting times when the violet laser was blocked. No attempt was made to further spectrally correct the observed fluorescence due to interference filter, monochromator grating, or PMT photocathode responsivity.

For temperature calibration, the stage was externally controlled (LakeShore Model 331). For each type of polymer composite sample, the temperature was step-wise changed, allowed to equilibrate, and the corresponding fluorescence ratio between the "trough" (≈465 nm) and the "peak" (≈479 nm) measured, from room temperature until above the $T_m$ of the particular polymer. The overall perylene fluorescence intensity decreased as the sample temperature was raised (**Figure 12**); in addition, the shape of the spectrum is altered resulting in an increase of the trough-to-peak ratio value. This ratio value was plotted versus the stabilized stage temperature to generate the specific polymer composite calibration curves for the each sample type as shown in Figure 1,2.

The overall experiment was computer-controlled by a user-written program (LabVIEW) to iteratively tune the monochromator, control the stage temperature, and sequentially measure both the fluorescence and laser amplitude.

*Photothermal Heating and Temperature-Sensing within the Polymer Matrix*: The outputs of two, 532 nm, continuous-wave diode lasers (100 mW and 150 mW) were primarily utilized for photothermal heating of the polymer samples. The laser beams were expanded using positive lenses and spatially aligned such that the spot size of the combined green beam completely overlapped the smaller-sized probe violet laser beam for all measurements. For the highest excitation intensities, the single-line 514 nm output of an argon-ion laser was utilized. Crossed linear polarizers in the green beam allowed the laser intensity to be varied without altering beam alignment; an optical power meter (Coherent Model Powermax PM10) measured the laser intensity just prior to the sample. Using this arrangement, the green laser acted to photothermally heat the samples via the gold nanoparticles, thus causing the observed reduction in fluorescence intensity and change
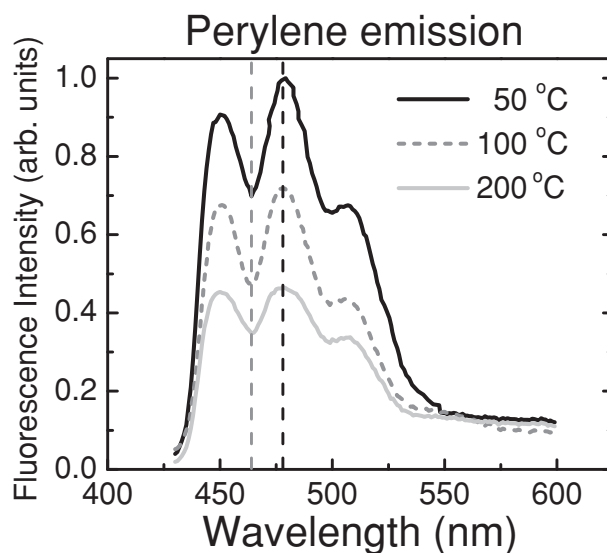


**Figure 12.** Normalized measured emission from a PAN composite film doped with 0.02 wt% perylene at three different temperatures attained by conventional heating. Vertical dashed lines indicate the spectral locations of the trough (465 nm) and peak (479 nm), respectively. No green light was present.

in emission spectrum shape of the nearby perylene molecules. An increase in temperature corresponded to an increase in the trough-to-peak ratio; comparing the measured ratio to the calibration curve of the specific polymer enabled determination of the bulk temperature of the sample. By sequentially measuring the fluorescence intensity at the trough and peak wavelength, the change in temperature of the sample via photothermal heating could be monitored versus time. For vacuum measurements, the samples were mounted inside a stainless steel chamber with fused silica viewports, and the fluorescence imaged to the monochromator via intra-vacuum optical components. The overall pressure of ≈$10^{-7}$ torr was achieved using a turbomolecular pump backed by an oil-free scroll pump.

## Supporting Information

Supporting Information is available from the Wiley Online Library or from the author.

## Acknowledgements

**FULL PAPER**

[1] M. C. Daniel, D. Astruc, *Chem. Rev.* **2004**, *104*, 293.

[2] A. N. Shipway, E. Katz, I. Willner, *ChemPhysChem* **2000**, *1*, 18.

[3] A. C. Templeton, M. P. Wuelfing, R. W. Murray, *Accounts Chem. Res.* **2000**, *33*, 27.

[4] W. A. Murray, W. L. Barnes, *Adv. Mater.* **2007**, *19*, 3771.

[5] P. V. Kamat, *J. Phys. Chem. B* **2002**, *106*, 7729.

[6] M. Pelton, J. Aizpurua, G. Bryant, *Laser Photonics Rev.* **2008**, *2*, 136.

[7] W. L. Barnes, A. Dereux, T. W. Ebbesen, *Nature* **2003**, *424*, 824.

[8] P. K. Jain, K. S. Lee, I. H. El-Sayed, M. A. El-Sayed, *J. Phys. Chem. B* **2006**, *110*, 7238.

[9] X. Wu, T. Ming, X. Wang, P. N. Wang, J. F. Wang, J. Y. Chen, *ACS Nano* **2010**, *4*, 113.

[10] J. Zhao, X. Y. Zhang, C. R. Yonzon, A. J. Haes, R. P. Van Duyne, *Nanomedicine* **2006**, *1*, 219.

[11] D. M. Adams, L. Brus, C. E. D. Chidsey, S. Creager, C. Creutz, C. R. Kagan, P. V. Kamat, M. Lieberman, S. Lindsay, R. A. Marcus, R. M. Metzger, M. E. Michel-Beyerle, J. R. Miller, M. D. Newton, D. R. Rolison, O. Sankey, K. S. Schanze, J. Yardley, X. Y. Zhu, *J. Phys. Chem. B* **2003**, *107*, 6668.

[12] C. A. Berven, M. N. Wybourne, L. Clarke, L. Longstreth, J. E. Hutchison, J. L. Mooster, *J. Appl. Phys.* **2002**, *92*, 4513.

[13] K. I. Bolotin, F. Kuemmeth, A. N. Pasupathy, D. C. Ralph, *Appl. Phys. Lett.* **2004**, *84*, 3154.

[14] L. Clarke, M. N. Wybourne, M. D. Yan, S. X. Cai, L. O. Brown, J. Hutchison, J. F. W. Keana, *J. Vac. Sci. Technol. B* **1997**, *15*, 2925.

[15] M. N. Wybourne, L. Clarke, M. D. Yan, S. X. Cai, L. O. Brown, J. Hutchison, J. F. W. Keana, *Jpn. J. Appl. Phys.* **1997**, *36*, 7796.

[16] M. N. Wybourne, J. E. Hutchison, L. Clarke, L. O. Brown, J. L. Mooster, *Microelectron. Eng.* **1999**, *47*, 55.

[17] M. B. Cortie, X. Xu, H. Chowdhury, H. Zareie, G. Smith, in *Plasmonic heating of gold nanoparticles and its exploitation*, **2005**, (Ed: F. A.-S. Said), SPIE, Bellingham, WA **2005**, pp 565–573.

[18] A. O. Govorov, H. H. Richardson, *Nano Today* **2007**, *2*, 30.

[19] X. H. Huang, P. K. Jain, I. H. El-Sayed, M. A. El-Sayed, *Lasers Med. Sci.* **2008**, *23*, 217.

[20] P. K. Jain, X. H. Huang, I. H. El-Sayed, M. A. El-Sayed, *Acc. Chem. Res.* **2008**, *41*, 1578.

[21] D. Pissuwan, S. M. Valenzuela, M. B. Cortie, *Trends Biotechnol.* **2006**, *24*, 62.

[22] E. Boisselier, D. Astruc, *Chem. Soc. Rev.* **2009**, *38*, 1759.

[23] Y. L. Luo, Y. S. Shiao, Y. F. Huang, *ACS Nano* **2011**, *5*, 7796.

[24] L. Paasonen, T. Laaksonen, C. Johans, M. Yliperttula, K. Kontturi, A. Urth, *J. Controlled Release* **2007**, *122*, 86.

[25] D. Pissuwan, T. Niidome, M. B. Cortie, *J. Controlled Release* **2011**, *149*, 65.

[26] A. G. Skirtach, C. Dejugnat, D. Braun, A. S. Susha, A. L. Rogach, W. J. Parak, H. Mohwald, G. B. Sukhorukov, *Nano Lett.* **2005**, *5*, 1371.

[27] W. I. Choi, J. Y. Kim, C. Kang, C. C. Byeon, Y. H. Kim, G. Tee, *ACS Nano* **2011**, *5*, 1995.

[28] E. S. Day, J. G. Morton, J. L. West, *J. Biomech. Eng.- Trans. ASME* **2009**, *131*, 5.

[29] H. C. Huang, K. Rege, J. J. Heys, *ACS Nano* **2010**, *4*, 2892.

[30] P. K. Jain, I. H. El-Sayed, M. A. El-Sayed, *Nano Today* **2007**, *2*, 18.

[31] B. Van de Broek, N. Devoogdt, A. D'Hollander, H. L. Gijs, K. Jans, L. Lagae, S. Muyldermans, G. Maes, G. Borghs, *ACS Nano* **2011**, *5*, 4319.

[32] S. T. Wang, K. J. Chen, T. H. Wu, H. Wang, W. Y. Lin, M. Ohashi, P. Y. Chiou, H. R. Tseng, *Angew. Chem. Int. Ed.* **2010**, *49*, 3777.

[33] E. Lukianova-Hleb, Y. Hu, L. Latterini, L. Tarpani, S. Lee, R. A. Drezek, J. H. Hafner, D. O. Lapotko, *ACS Nano* **2010**, *4*, 2109.

[34] E. Y. Lukianova-Hleb, L. J. E. Anderson, S. Lee, J. H. Hafner, D. O. Lapotko, *Phys. Chem. Chem. Phys.* **2010**, *12*, 12237.

[35] S. Link, C. Burda, M. B. Mohamed, B. Nikoobakht, M. A. El-Sayed, *J. Phys. Chem. A* **1999**, *103*, 1165.

[36] C. D. Jones, L. A. Lyon, *J. Am. Chem. Soc.* **2003**, *125*, 460.

[37] I. Alessandri, L. E. Depero, *Nanotechnology* **2008**, *19*, 7.

[38] M. B. Cortie, N. Harris, M. Ford, *Phys. B-Condensed Matter* **2007**, *394*, 188.

[39] H. H. Richardson, Z. N. Hickman, A. O. Govorov, A. C. Thomas, W. Zhang, M. E. Kordesch, *Nano Lett.* **2006**, *6*, 783.

[40] K. Vanherck, S. Hermans, T. Verbiest, I. Vankelecom, *J. Mater. Chem.* **2011**, *21*, 6079.

[41] S. Maity, L. N. Downen, J. R. Bochinski, L. I. Clarke, *Polymer* **2011**, *52*, 1674.

[42] A. J. Bur, M. G. Vangel, S. Roth, *Appl. Spectrosc.* **2002**, *56*, 174.

[43] R. A. Domingues, I. V. P. Yoshida, T. D. Z. Atvars, *J. Polym. Sci. Part. B-Polym. Phys.* 48, 74.

[44] R. D. Priestley, C. J. Ellison, L. J. Broadbelt, J. M. Torkelson, *Science* **2005**, *309*, 456.

[45] O. Schurr, S. B. Yamaki, C. H. Wang, T. D. Z. Atvars, R. G. Weiss, *Macromolecules* **2003**, *36*, 3485.

[46] L. M. Liz-Marzan, *Langmuir* **2006**, *22*, 32.

[47] C. C. Chang, C. M. Huang, Y. H. Chang, C. S. Kuo, *Opt. Express* **2010**, *18*, A174.